Electronic Supplementary Material (ESI) for Chemical Communications.

Table S1. Summary of the histogram analysis

State	Stage	D_{cc} (nm)	Number of molecules analyzed	Number of frames analyzed
Closed state of $MyD88^{FL}$ (WT)	Mica surface	3.40 ± 0.02	30	1500
Open state of $MyD88^{FL}$ (WT)	Mica surface	5.08 ± 0.04		
$MyD88^{FL}$ (EQ)	Mica surface	5.49 ± 0.04	30	1500
Closed state of $MyD88^{FL}$ (WT)	APTES-modified mica	3.66 ± 0.02	30	1500
Open state of $MyD88^{FL}$ (WT)	APTES-modified mica	5.30 ± 0.04		
Dominant state of $MyD88^{FL}$ (RA)	APTES-modified mica	4.70 ± 0.03	30	1500
Minor state of $MyD88^{FL}$ (RA)	APTES-modified mica	6.91 ± 0.04		

D_{cc} values are shown as the mean ± SEM.

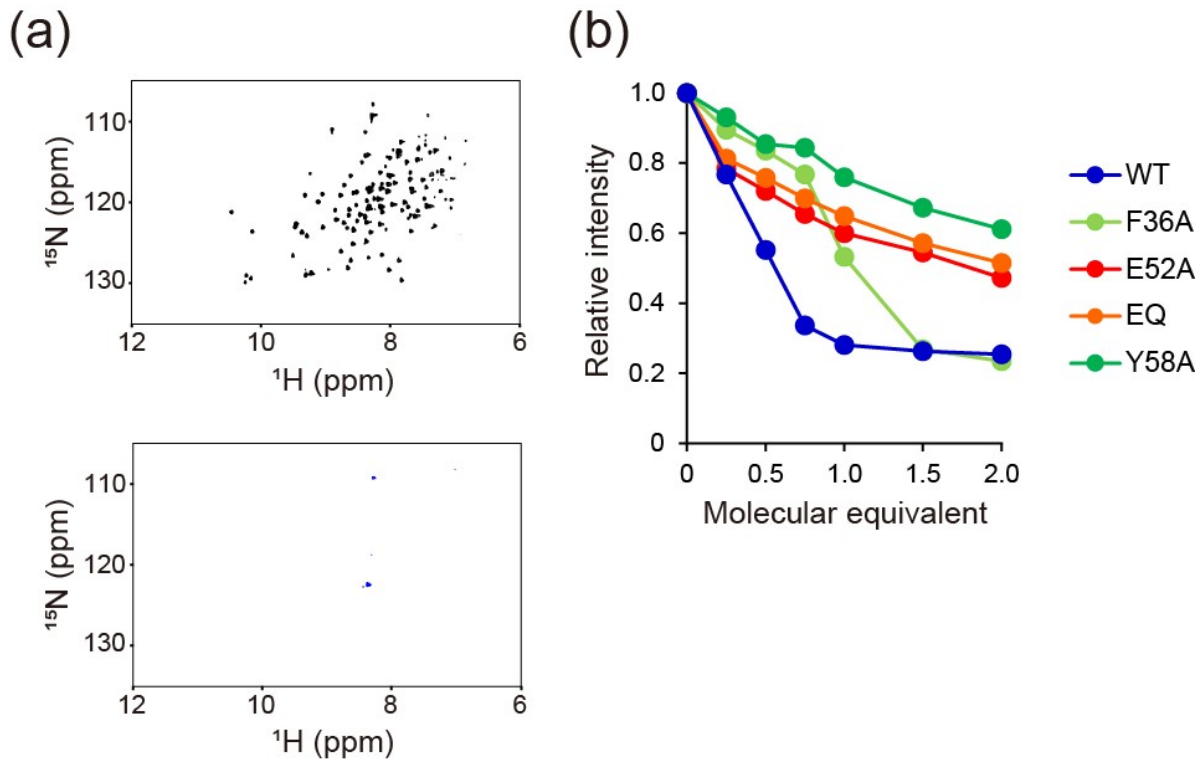

Figure S1. NMR titration experiments to identify the binding sites of DD_{MyD88} for $^{15}N\text{-}TIR_{MyD88}$.

(a) $^{1}H\text{-}^{15}N$ SOFAST-HMQC spectra of $^{15}N\text{-}TIR_{MyD88}$ without (top) and with (bottom) 2 eq. of DD_{MyD88}. (b) Plot of the relative intensities of the NMR signals of $^{15}N\text{-}TIR_{MyD88}$ titrated with DD_{MyD88} variants. The relative intensity was calculated as the ratio of the integrated value of the peak intensity from 6.0 ppm to 12.0 ppm at each titration point relative to that of the DD_{MyD88} free state in the ^{1}H 1D projected spectra. The attenuation of WT (blue) and F36A (yellow-green) was saturated before the addition of two molecular equivalents DD_{MyD88}, while that of E52A (red), EQ (E52Q-E53Q-D55N) (orange) and Y58A (green) was not. The weak attenuation suggests that these mutations (E52A, EQ and Y58A) inhibited the interaction between DD_{MyD88} and $^{15}N\text{-}TIR_{MyD88}$.

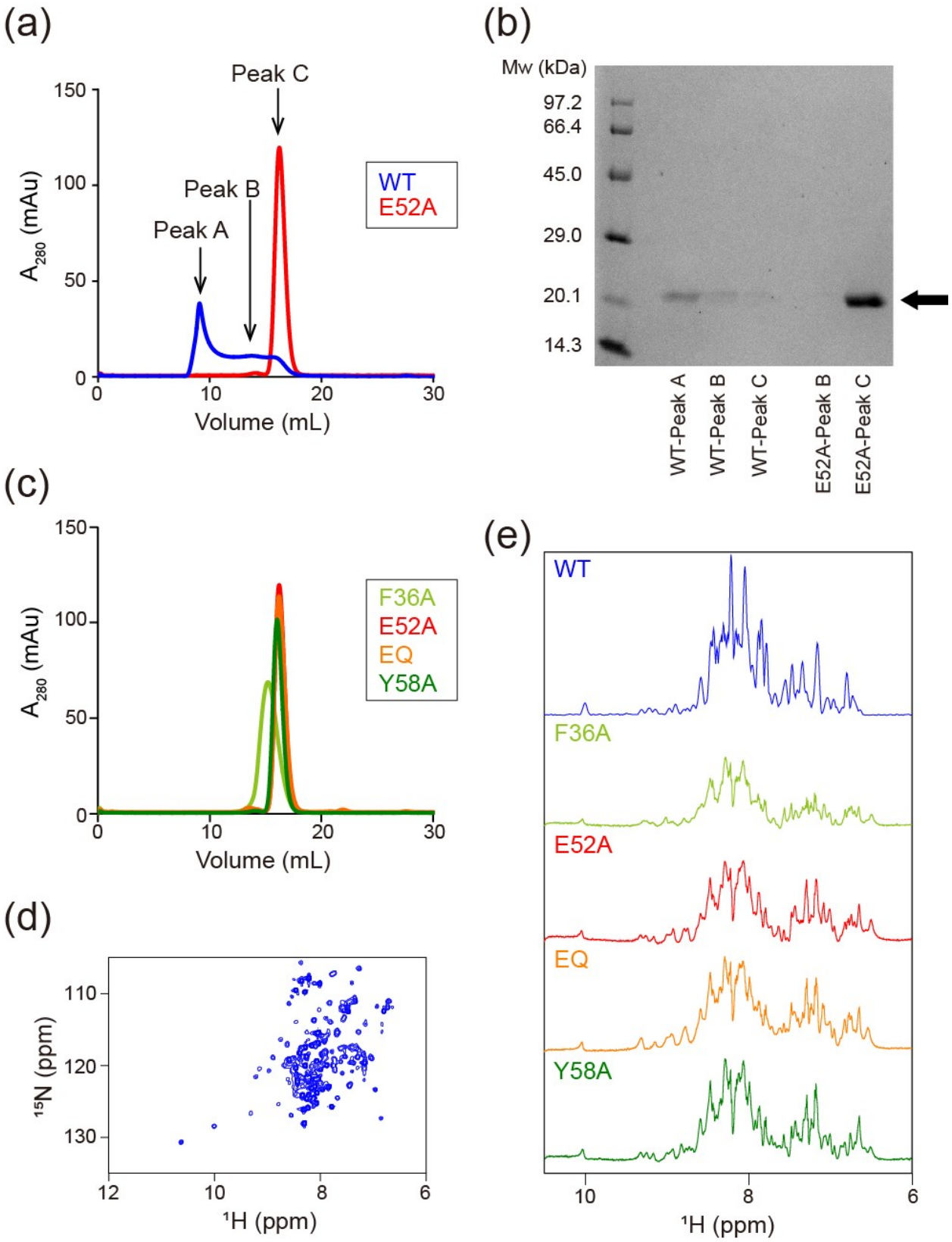

Figure S2. The global characters of DD_{MyD88} (WT) and mutants.

(a) Size-exclusion chromatograms of DD_{MyD88} (WT) (blue) and DD_{MyD88} (E52A) (red). The analysis was performed on 100 μM DD_{MyD88} samples with a Superdex 200 10/300 GL column in a buffer containing 20 mM

potassium phosphate (pH 6.0), 150 mM NaCl and 10 mM dithiothreitol. The extremely broadened peak of DD_{MyD88} (WT) suggests the formation of complexes of various molecular weights, while the introduction of the E52A mutation led to dissociation of the complexes. The estimated size of DD_{MyD88} (E52A) from the profile roughly corresponds to a dimer. (b) SDS-PAGE showed that DD_{MyD88} (WT) was present in most of the fractions. (c) Size-exclusion chromatograms of DD_{MyD88} mutants (F36A; yellow green, E52A; red, EQ; orange and Y58A; green). The analysis was performed under the same conditions as in (a). The chromatograms suggest that all DD_{MyD88} mutations led to the dissociation of the various molecular weight complexes (2-4-mers). (d) ^{1}H-^{15}N SOFAST-HMQC spectra of ^{15}N-DD_{MyD88} (WT) measured in the same buffer conditions as in Fig. S1a. (e) Comparison between the ^{1}H 1D projected spectra of (d) and the ^{1}H 1D spectra of DD_{MyD88} mutants. The lack of a marked difference between the spectra of the WT and mutants suggests that all mutants formed a similar conformation to the WT.

DD_{MyD88} was previously demonstrated to form self-associated oligomers in solution in a reversible manner.[1,2] Although structures of oligomers exclusively formed by DD_{MyD88} have not been determined, the crystal structure of the complex comprising DD_{MyD88}, DD_{IRAK4} and DD_{IRAK2} provided critical insights into the self-oligomers of DD_{MyD88},[3] in which six copies of DD_{MyD88} assembled continuously to form a helical ring. Although the tetramer-like side of the ring was bound by DD_{IRAK4} (Fig. S3b), the hexamer was largely held together via self-associative interactions between multiple DD_{MyD88}. According to this observation, DD_{MyD88} should have a propensity to form self-associated oligomers in solution. The concentration of DD_{MyD88} in our NMR titration experiments was 10-100 μM. At this concentration, DD_{MyD88} begins to form self-oligomers as DD_{MyD88} was shown to exist as monomers at concentrations less than 0.4 mg/ml (~27 μM) but to begin to form self-oligomers at higher concentrations.[1] Consistent with this report, we also observed the emergence of larger oligomers of DD_{MyD88} at 100 μM (Fig. S2a). Thus in our NMR titration, DD_{MyD88} would have existed as such self-oligomers. Consistently, all the mutated DD_{MyD88} we created, which had mutations at the homotypic DD-DD interface of the DD_{MyD88} hexamer in the crystal structure, showed substantial decreases in self-associative nature and existed as 2-4-mers (Fig. S2a-c), indicating that the DD_{MyD88} oligomer we observed in solution is closely related to that in the crystal.

Widespread disappearance of NMR signals by itself cannot discriminate functionally relevant interactions from nonspecific aggregations. Nevertheless, from the words above, we interpreted the disappearance of NMR signals in our titration experiment to be due to the interaction between ^{15}N-TIR_{MyD88} and functionally relevant oligomeric states of DD_{MyD88}, which thus reflects the functional significance of MyD88.

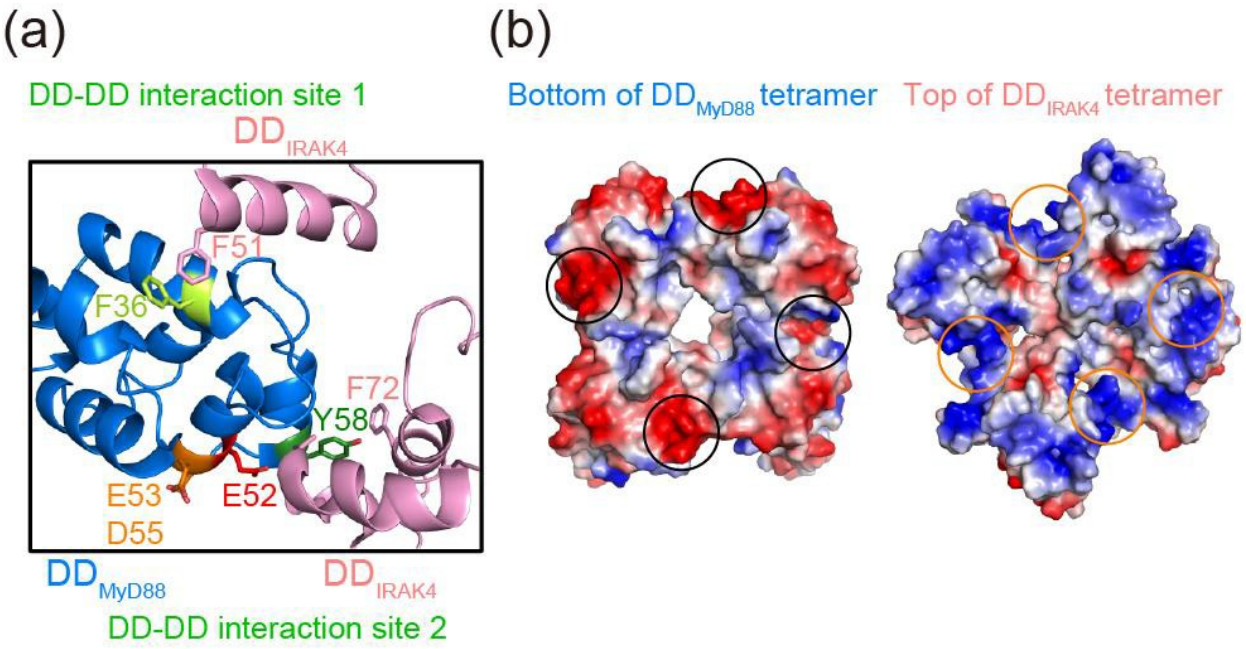

Figure S3. Interaction sites between DD_{MyD88} and DD_{IRAK4}.

(a) Interaction sites between DD_{MyD88} and DD_{IRAK4} in the structure of the DD oligomer (PDB ID: 3MOP).[3] (b) Charge distribution of interaction surfaces between the DD_{MyD88} tetramer and the DD_{IRAK4} tetramer (PDB ID: 3MOP). Anionic sites formed by E52, E53 and D55 indicated by black circles on the DD_{MyD88} tetramer played important roles in interacting with cationic sites on DD_{IRAK4} (orange circles).

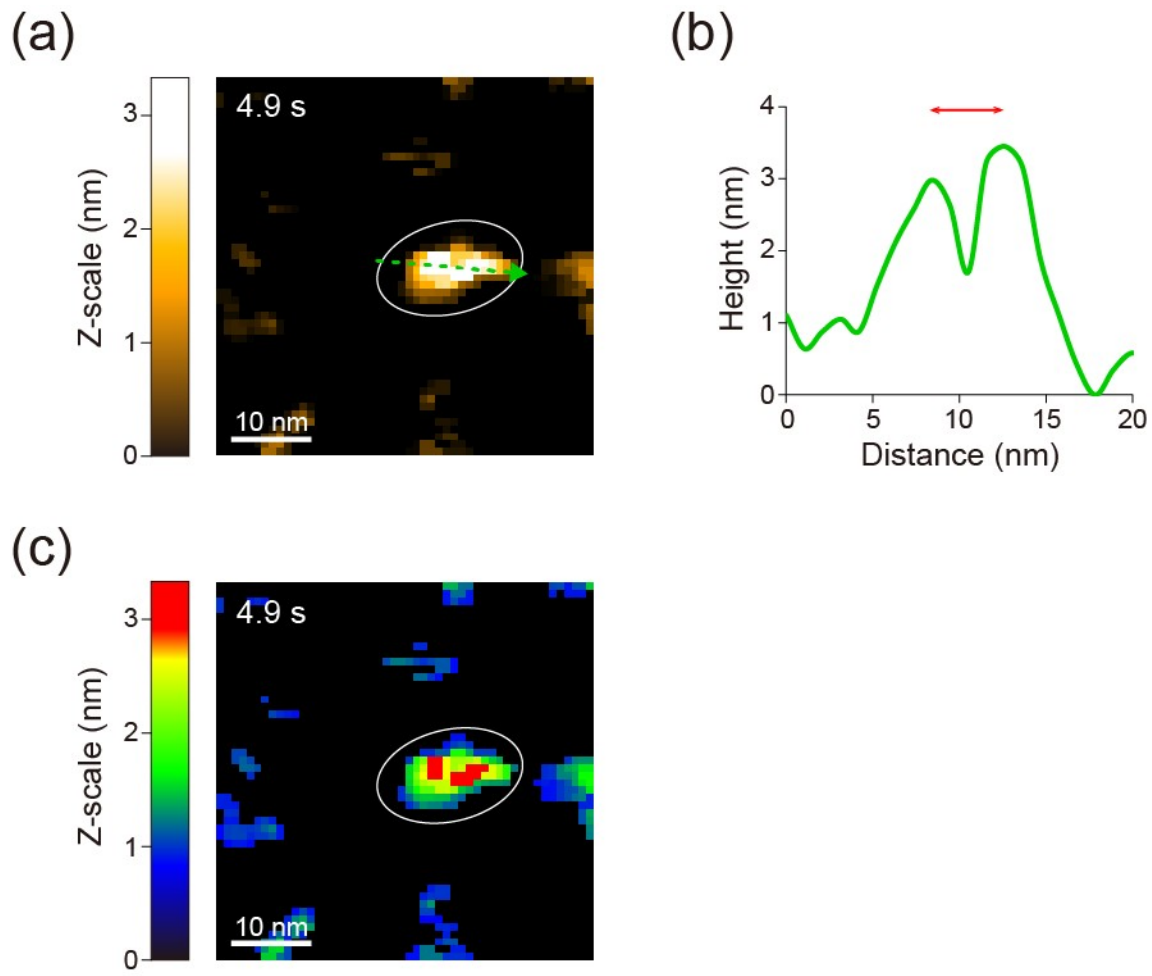

Figure S4. The distinction between two subparticles in the closed state in the AFM image.

(a) Representative HS-AFM images of $MyD88^{FL}$ in the closed state recorded on APTES-modified micas. (Frame rate, 50 ms/frame; scan area, 50 × 50 nm^2 with 50 × 50 pixels; Z-scale, 4.3 nm; scale bars, 10 nm.) The sectional view of the green arrow in the AFM image (b) and the image with the color scale changed from black-yellow to multicolor (c) show that the image visualized as the single subparticle in (a) consisted of two particles.

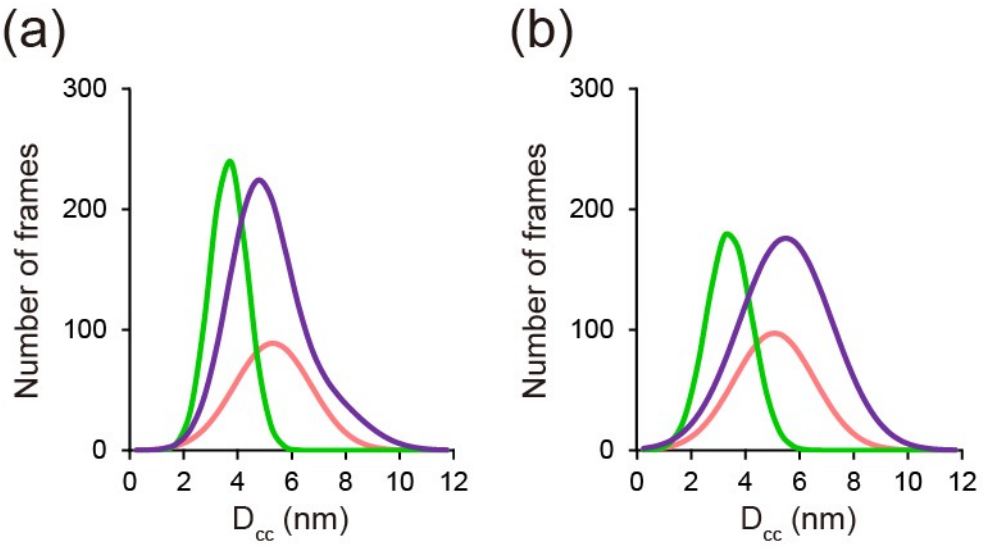

Figure S5. Comparison of the fitting curves of histograms.

Green, pink and purple curves corresponding to the fitting curves shown in Fig. 3e-h. The curves correspond to the APTES-modified mica surface (a) or the mica surface (b). Both overlaid fitting curves show that the mutants predominantly adopted the open state of $MyD88^{FL}$.

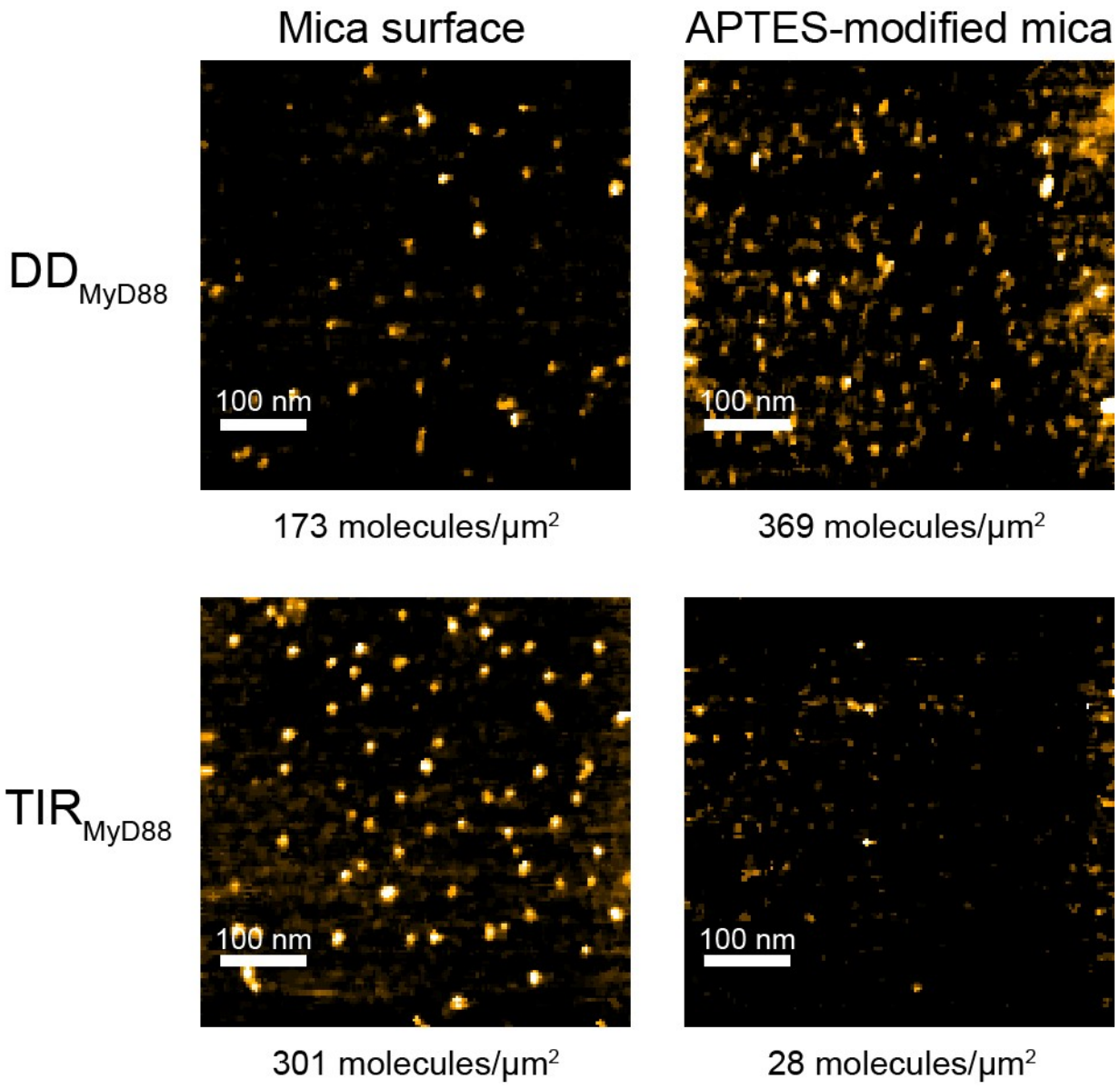

Figure S6. Unmodified and APTES-modified mica surfaces adsorbed DD_{MyD88} and TIR_{MyD88} with different efficiencies.

HS-AFM images recorded with 10 nM isolated DD_{MyD88} on a mica surface (top left) or an APTES-modified mica surface (top right) and with 10 nM isolated TIR_{MyD88} on a mica surface (bottom left) or an APTES-modified mica surface (bottom right). Frame rate, 600 ms/frame; scan area, 500 × 500 nm^2 with 150 × 150 pixels; Z-scale, 4.5 nm; scale bars, 100 nm.

In AFM experiments, protein samples need to be weakly attached to AFM stages, which largely rely on electrostatic adsorption onto the surface of the stages. Considering the isoelectric points of DD_{MyD88} (theoretical pI = 4.57) and TIR_{MyD88} (theoretical pI = 8.97), either of the two domains in $MyD88^{FL}$ may dominantly attach to the stage depending on the electrostatic properties of the surface. This situation may cause inhomogeneous attachment at the molecular level on the surface, which can generate artefacts, especially in experiments using a series of MyD88 derivatives, since amino acid substitutions may change the charges of the domains, altering the adsorption mode of the molecules.

To alleviate such artefacts, we employed two different AFM stages, unmodified mica and mica modified with APTES, for different MyD88^{FL} derivatives. The former is negatively charged, while the latter is positive. Hence, as shown in the figures above, the APTES-modified mica adsorbed more DD_{MyD88}, while the unmodified mica adsorbed more TIR^{MyD88}. Thus, we used the former for examining the MyD88^{FL} derivatives harboring substitutions in TIR_{MyD88}, as the surface is expected to adsorb DD_{MyD88} of MyD88^{FL}, leaving TIR_{MyD88} of MyD88^{FL} free to move regardless of whether substitutions are introduced. For a similar reason, we used unmodified mica to examine substitutions in DD_{MyD88} of MyD88^{FL}, as the surface is expected to adsorb TIR_{MyD88} of MyD88^{FL}, leaving DD_{MyD88} mobile. It should be noted that the HS-AFM results for MyD88^{FL} (WT) recorded on these two distinct surfaces were indeed consistent with each other (see Fig. 3e and 3f).

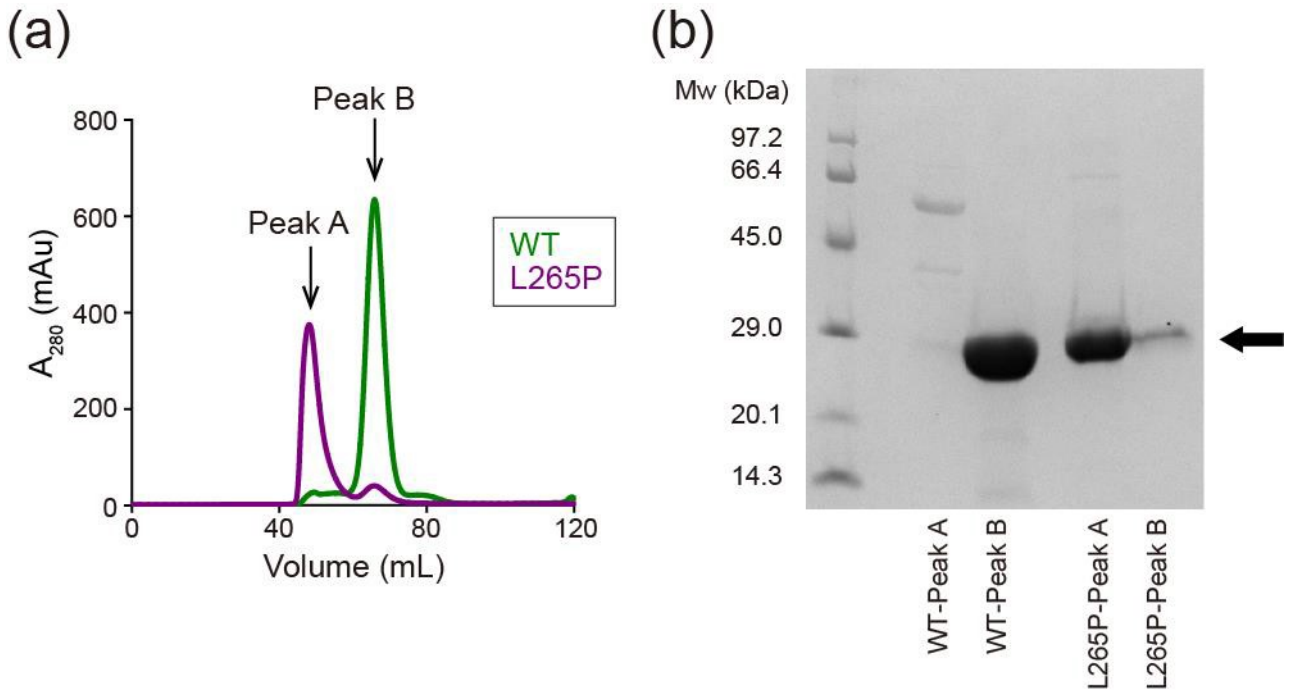

Figure S7. His-GB1-TIR$_{MyD88}$ aggregation shown by chromatography.

(a) Size-exclusion chromatograms of His-GB1-TIR$_{MyD88}$ (WT) (green) and His-GB1-TIR$_{MyD88}$ (L265P) (purple). The His-GB1-TIR$_{MyD88}$ (L265P) eluted essentially in the void region, suggesting that the protein was mostly aggregated. (b) SDS-PAGE analysis showed that most of the His-GB1-TIR$_{MyD88}$ (L265P) eluted in Peak A, while His-GB1-TIR$_{MyD88}$ (WT) eluted in Peak B. The position of Peak B corresponds to monomeric His-GB1-TIR$_{MyD88}$.

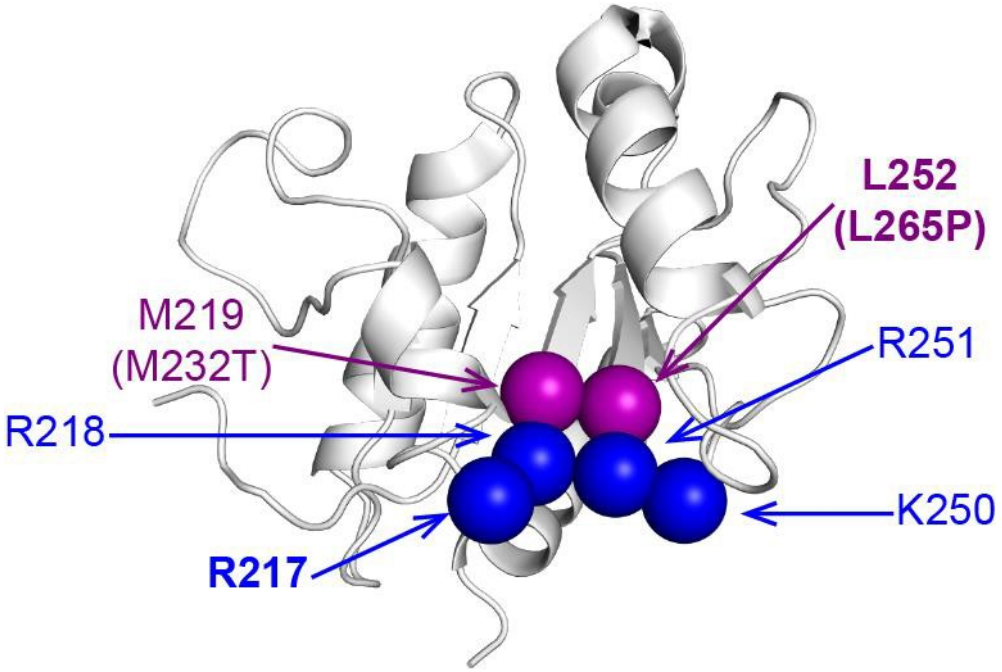

Figure S8. Position of pathogenic mutations and the intramolecular interaction site on TIR_{MyD88} (PDB ID: 2Z5V).

Two mutations of TIR_{MyD88}, M232T and L265P (purple spheres), were reported as pathogenic mutations in lymphomas.[4] These mutated residues neighbor four cationic residues (R217, R218, K250 and K251) identified in this study as the intramolecular DD-TIR interaction site of MyD88 (blue spheres). Their proximity implies that the pathogenic mutations could abolish the intramolecular DD-TIR interaction of MyD88, contributing to the constitutive activation of MyD88-dependent signaling as observed in the reported lymphomas.

Movie S1. Representative HS-AFM movie of a $MyD88^{FL}$ molecule.

Frame rate, 100 ms/frame (play back rate, 100 ms/frame); scan area, 100 × 100 nm2 with 100 × 100 pixels; Z-scale, 4.3 nm. Related to Fig. 3.

Supplemental Material and Method

Construction of expression vectors

The coding region of $MyD88^{FL}$ (MyD88, NM_002468.4, residues 14-309, annotated as 1-296 in this study) was amplified from the human cDNA library by polymerase chain reaction and cloned into a pET-28a vector [Novagen, WI, USA], which was engineered with a 10×His-tagged N-terminal small ubiquitin-like modifier (SUMO)-3 (NM_006936.2, residues 14-92) for protein expression and purification. The plasmids for DD_{MyD88} (residues 1-152) and TIR_{MyD88} (residues 153-296) were derived from the $MyD88^{FL}$ construct. The plasmid of DD_{MyD88} was cloned into a pGEX-6P-1 vector [GE Healthcare, IL, USA], and the plasmid of TIR_{MyD88} was cloned into a pET-28a vector, which was engineered with a 6×His-tagged Streptococcal protein GB1 domain (GB1) (residues 261-324). The constructs for the derivatives, such as the alanine-substituted derivatives, were prepared by site-directed mutagenesis.

Protein expression and purification

For experimental samples, the expression vector for either the His-GB1 tag fusion TIR_{MyD88}, GST tag fusion DD_{MyD88} or His-SUMO tag fusion $MyD88^{FL}$ was transformed into *E. coli* BL21(DE3) cells. For isotope labeling, the cells transformed with the His-GB1 tag fusion TIR_{MyD88} vector were grown in either M9 minimal medium containing $^{15}NH_4Cl$ or a premixed medium, *E.coli* OD1 DN [Silantes GmbH, Bayern, Germany]. The cells transformed with the GST tag fusion DD_{MyD88} vector or His-SUMO tag fusion $MyD88^{FL}$ vector were grown in LB medium. The His-GB1 tag fusion TIR_{MyD88} and GST tag fusion DD_{MyD88} were first purified with affinity column chromatography. After removal of each tag with GST-HRV3C, the protein was further purified with ion exchange chromatography and size-exclusion chromatography.

The His-SUMO tag fusion $MyD88^{FL}$ was expressed as inclusion bodies. The washed cell debris was resuspended with denaturation buffer containing 50 mM Tris-HCl (pH 8.0), 300 mM NaCl and 6 M guanidine chloride. The denaturated His-SUMO tag fusion $MyD88^{FL}$ was purified with affinity column chromatography. Eluted His-SUMO tag fusion $MyD88^{FL}$ was refolded by the rapid dilution method with ten times volume dilution buffer containing 20 mM Tris-HCl (pH 8.0), 300 mM NaCl, 400 mM arginine chloride and 20 mM dithiothreitol. After removal of the His-SUMO tag with GST-SENP2, refolded $MyD88^{FL}$ was further purified with size-exclusion chromatography.

NMR spectroscopy

NMR spectra were measured by Bruker Avance II 700 MHz and Avance II 800 MHz spectrometers equipped with cryogenic probes [Bruker, MA, USA] at 298 K. The samples for NMR analyses were dissolved in NMR buffer containing 20 mM potassium phosphate (pH 6.0), 150 mM NaCl, and 10 mM DTT with the addition of 5 v/v % D_2O. To detect the interaction between TIR and DD, 10 μL of 300 μM unlabeled DD or its derivatives in NMR buffer was added to 240 μL of 50 μM [^{1}H, ^{15}N]-TIR.

For transferred cross-saturation (TCS) experiments, a sample containing 65 μM [^{2}H,^{15}N]-TIR and 6.5 μM DD was dialyzed by RE buffer containing 20 mM potassium phosphate (pH 6.0), 150 mM NaCl, 50 mM Arg-HCl, 50 mM Glu-NaOH, 10 mM DTT and 80 v/v% D_2O. The TCS experiments was conducted in accordance with a previously reported procedure.[5] The maximum RF amplitude was 0.17 kHz for WURST-2 (adiabatic factor Q0

= 1). The saturation frequency was set at 0.9 p.p.m. The measurement times were 65 h with a recycle delay of 4.5 s [3.0 s for the adjusting delay and 1.5 s for the saturation time]. All spectra were processed via NMRPipe [6] or Bruker TopSpin 3.5 (Bruker) and analyzed using Sparky.[7]

High-speed AFM imaging

A high-speed atomic force microscope (HS-AFM) was equipped with a small cantilever (BL-AC10-DS-A2 [Olympus, Tokyo, Japan]: spring constant, k = 0.1 N/m, resonance frequency, f = 400~500 kHz in water) and was operated in tapping mode at room temperature.[8–10] An amorphous carbon tip was grown on the top of each cantilever by electron-beam deposition with a scanning electron microscope (ERA-8000FE [Elionix, Tokyo, Japan]). The free oscillation amplitude was 1.4~2 nm, and the typical set-point amplitude was 85% of the free oscillation amplitude. A mica disk (1 mm in diameter) fixed by epoxy glue on a glass rod (2 mm in diameter and 2 mm in height) was used as a sample stage.[9] Before or after the sample stage was fixed by nail polish on the z-piezo of the HS-AFM scanner, the mica was freshly cleaved. Freshly cleaved mica and AP-mica were used as substrates. AP-mica was prepared by depositing 0.05% 3-aminopropyltriethoxysilane (Shin-Etsu Chemical) on freshly cleaved mica and left for 3 min.[11] Then, 5 μL of 10 nM MyD88^{FL} (WT) or its derivatives was adsorbed on the substrates in AFM sample buffer containing 20 mM MES-NaOH (pH 6.0) and 10 mM DTT. After 5 min, the sample was rinsed with 20 μL of sample buffer.

Processing of HS-AFM data

The HS-AFM image sequences were processed using ImageJ software ver. 1.50i (imagej.nih.gov/ij/), additional plugins for ImageJ (https://imagej.nih.gov/ij/plugins/) and Kodec 4.5.7.25 developed by the Kanazawa-Univ Bio-AFM Frontier Research Center.[12] All images applied polynomial fitting in both the x- and y-direction and median filter in 1.0 pixel, and adjusted the background height level to zero after background leveling.[13]
D_{cc} was measured and analyzed by the ImageJ plugin, MTrackJ (imagescience.org/meijering/software/mtrackj/). The collected data were processed with Excel 2010 [Microsoft, WA, USA] and R (r-project.org/index.html).

Supplemental Reference

1 P. G. Motshwene, M. C. Moncrieffe, J. G. Grossmann, C. Kao, M. Ayaluru, A. M. Sandercock, C. V. Robinson, E. Latz and N. J. Gay, *J. Biol. Chem.*, 2009, **284**, 25404–25411.

2 T. Yamamoto, N. Tsutsumi, H. Tochio, H. Ohnishi, K. Kubota, Z. Kato, M. Shirakawa and N. Kondo, *Mol. Immunol.*, 2014, **58**, 66–76.

3 S. C. Lin, Y. C. Lo and H. Wu, *Nature*, 2010, **465**, 885–890.

4 V. N. Ngo, R. M. Young, R. Schmitz, S. Jhavar, W. Xiao, K. H. Lim, H. Kohlhammer, W. Xu, Y. Yang, H. Zhao, A. L. Shaffer, P. Romesser, G. Wright, J. Powell, A. Rosenwald, H. K. Muller-Hermelink, G. Ott, R. D. Gascoyne, J. M. Connors, L. M. Rimsza, E. Campo, E. S. Jaffe, J. Delabie, E. B. Smeland, R. I. Fisher, R. M. Braziel, R. R. Tubbs, J. R. Cook, D. D. Weisenburger, W. C. Chan and L. M. Staudt, *Nature*, 2011, **470**, 115–121.

5 H. Takahashi, T. Nakanishi, K. Kami, Y. Arata and I. Shimada, *Nat. Struct. Biol.*, 2000, **7**, 220–223.

6 F. Delaglio, S. Grzesiek, G. W. Vuister, G. Zhu, J. Pfeifer and A. Bax, *J. Biomol. NMR*, 1995, **6**, 277–293.

7 W. Lee, W. M. Westler, A. Bahrami, H. R. Eghbalnia and J. L. Markley, *Bioinformatics*, 2009, **25**, 2085–2087.

8 T. Ando, N. Kodera, D. Maruyama, E. Takai, K. Saito and A. Toda, *Jpn. J. Appl. Phys.*, 2002, **41**, 4851–4856.

9 T. Uchihashi, N. Kodera and T. Ando, *Nat. Protoc.*, 2012, **7**, 1193–1206.

10 T. Watanabe-Nakayama, M. Itami, N. Kodera, T. Ando and H. Konno, *Sci. Rep.*, 2016, **6**, 1–11.

11 D. Yamamoto, A. Taoka, T. Uchihashi, H. Sasaki, H. Watanabe, T. Ando and Y. Fukumori, *Proc. Natl. Acad. Sci.*, 2010, **107**, 9382–9387.

12 K. X. Ngo, N. Kodera, E. Katayama, T. Ando and T. Q. Uyeda, *Elife*, 2015, **2015**, 1–22.

13 K. O. Takahiro Watanabe-Nakayama, *Nanoscale imaging*, Human Press, 2018.